Interfacial Self-Assembly of Polyelectrolyte-Capped Gold Nanoparticles

Honghu Zhang,[†] Srikanth Nayak,[‡] Wenjie Wang,[¶] Surya Mallapragada,[‡] and David Vaknin[*,§]

†*Ames Laboratory, and Department of Materials Science and Engineering, Iowa State University, Ames,Iowa 50011, United States*

‡*Ames Laboratory, and Department of Chemical and Biological Engineering, Iowa State University, Ames, Iowa 50011, United States*

¶*Division of Materials Sciences and Engineering, Ames Laboratory, USDOE, Ames, Iowa 50011, United States*

§*Ames Laboratory, and Department of Physics and Astronomy, Iowa State University, Ames, Iowa 50011, United States*

E-mail: vaknin@ameslab.gov

Abstract

We report on pH- and salt-responsive assembly of nanoparticles capped with polyelectrolytes at vapor-liquid interfaces. Two types of alkylthiol-terminated poly(acrylic acid) (PAAs, varying in length) are synthesized and used to functionalize gold nanoparticles (AuNPs) in order to mimic similar assembly effects of single-stranded DNA-capped AuNPs using synthetic polyelectrolytes. Using surface-sensitive X-ray scattering techniques, including grazing incidence small-angle X-ray scattering (GISAXS) and X-ray reflectivity (XRR), we demonstrate that PAA-AuNPs spontaneously migrate to the vapor-liquid interfaces and form Gibbs monolayers by lowering the pH of the suspension. The Gibbs monoalyers show chain-like structures of mono-particle thickness.

The pH-induced self-assembly is attributed to the protonation of carboxyl groups and to hydrogen bonding between the neighboring PAA-AuNPs. In addition, we show that adding $MgCl_2$ to PAA-AuNPs suspensions also induces adsorption at the interface, and that the strong affinity between magnesium ions and carboxyl groups leads to 2D and 3D clusters that yield partial surface coverage and poorer ordering of NPs at the interface. We also examine the assembly of PAA-AuNPs in the presence of a positively charged Langmuir monolayer that promotes the attraction of the negatively charged capped NPs by electrostatic forces. Our results show that synthetic polyelectrolyte-functionalized nanoparticles exhibit similar interfacial self-assembly behavior as that of DNA-functionalized nanoparticles providing a pathway for nanoparticle assembly in general.

Introduction

Polyelectrolytes have been widely used to fabricate functional materials owing to their inherent electrostatic, steric and other interactions that facilitate diverse self-assembly morphologies[1] where immense efforts have been devoted to functionalize planar and particulate substrates with polyelectrolytes.[2–4] Controllable and well-defined polyelectrolyte deposition or coating allows for potential applications in the fields of optics, catalysis, energy and bioengineering.[5–9] For instance, a layer-by-layer (LbL) assembly method has been developed for constructing multilayer functional thin films using sequential coating of oppositely charged polyelectrolytes on solid substrates or particles exploiting electrostatic forces.[3,4,10–12] Similar strategies have been exploited in the self-assembly of NPs at fluid-fluid interfaces to stabilize emulsions and foams, to create nanoporous membranes for filtration and encapsulation, and for fabrication of tunable opto-electro-magnetic metamaterials assemblies.[13–19] The advantage of coating with polyelectrolytes is that it is relatively simple, tunable, and versatile for building nanoscale structures for applications in devices. In addition, polyelectrolytes are diverse as synthetic ones[3,4] and also natural ones, most important of which are DNA and pro-

teins that have been exploited for their specific interactions in programmable assembly strategies.[20–25] Particularly, single-stranded DNA (ssDNA) functionalization of gold nanoparticles (AuNPs) through thiol-gold chemistry has been extensively used for self-assembly of various super-structures.[26–32] The unique hybridization ability of complementary ssDNA has led to programmable self-assembly of nanoparticles into remarkable three-dimensional (3D) superlattices of various lattice types. This has been further expanded by combining the functionalization of AuNPs into DNA origami frameworks.[33–36] Recently, DNA-AuNPs have been reported to assemble into two-dimensional (2D) ordered structures on liquid surfaces induced by salts[37–39] or templated by charged Langmuir monolayers.[40–42] Compared to 3D self-assembly, the simpler 2D systems not only provide an alternative platform to investigate general mechanisms of self-assembly, but also can be produced on macroscopic scales that are industrially viable and robust for future applications.[43–47] Previous studies in our group have shown that salts-induced 2D self-assembly of ssDNA-AuNPs at the vapor–liquid interface is driven by the overall hydrophobicity that arises from tunable amphiphilic character of alkylthiol-terminated ssDNA in the presence of counterions, such as Mg^{2+} that lower the hydrophilic character of DNA.[39] The experimental observations and theoretical considerations suggest that the essential function of ssDNA in the 2D assembly systems is polyelectrolytic in nature. To generalize our findings, we synthesize thiolated polyelectrolytes, i.e., alkylthiol-terminated poly(acrylic acid) (PAA) and functionalize AuNPs with PAA to assemble the capped NPs by manipulating the suspension conditions, namely, varying pH and salt concentrations. Figure 1 illustrates conceptually the similarity between functionalization with ssDNA and PAA. Synchrotron-based surface-sensitive X-ray scattering techniques including grazing incidence small-angle X-ray scattering (GISAXS) and X-ray reflectivity (XRR) are employed to monitor the self-assembly and structure of PAA-AuNPs at vapor–liquid interfaces. In addition to using counterions, we tune the pH of the PAA-AuNPs solutions to neutralize the charged groups to drive the PAA-AuNPs to the interface, and more importantly, to induce hydrogen bonding among neighboring PAAs that can lead to more robust

superstructures.

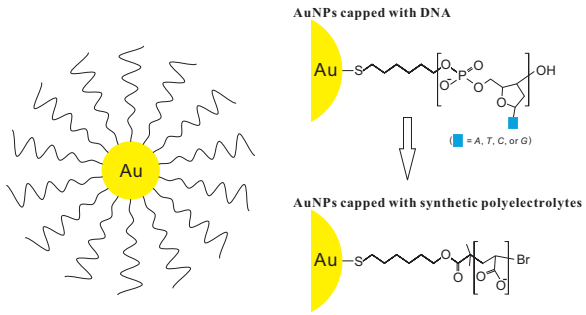

Figure 1: Schematic of mimicking DNA-capped gold nanoparticles (AuNPs) with AuNPs capped with synthetic polyelectrolytes, i.e., poly(acrylic acid).

Experimental Methods

Reagents and Materials

Citrate-stabilized gold nanoparticles of nominal 10 nm diameter were purchased from Ted Pella. 6-mercapto-1-hexanol ($HO-(CH_2)_6-SH$), 9-mercapto-1-nonanol ($HO-(CH_2)_9-SH$), *tert*-butyl acrylate (tBA), N, N, N', N'', N''-pentamethyldiethylenetriamine (PMDETA), copper(I) bromide (CuBr), triethylamine and α-bromoisobutyryl bromide (BiBB) were purchased from Sigma-Aldrich. Immobilized tris(2-carboxyethyl)phosphine (TCEP) disulfide reducing gel and magnesium chloride hexahydrate ($MgCl_2 \cdot 6\,H_2O$) was purchased from Thermo Fisher Scientific. 1,2-dihexadecanoyl-3-trimethylammonium-propane (DPTAP) was purchased from Avanti Polar Lipids.

Synthesis of PAA-Thiol: Alkylthiol-terminated poly(acrylic acid) ($PAA-R-SH$, $R = -(CH_2)_6-$ or $-(CH_2)_9-$) are synthesized as disulfides through Cu^+ catalyzed atom transfer radical polymerization (ATRP) as described elsewhere.[48,49] As shown in Fig. 2, $HO-R-SH$ is oxidized into disulfide by bromine, followed by a reaction with BiBB in the presence of triethylamine to obtain the ATRP initiator, $[Br(CH_3)_2C-COO-R-S]_2$. Copper catalyzed ATRP of tBA (80 mmol) is carried out in a two-necked Schlenk flask with the initiator (0.8 mmol), CuBr (1.6 mmol) and PMDETA (3.2 mmol) in 20 mL toluene as the solvent. The

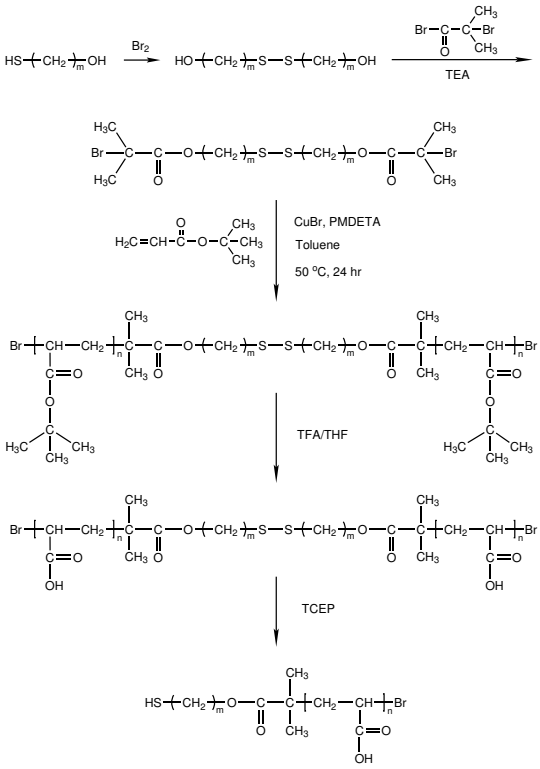

Figure 2: The reaction scheme for synthesis of PAA-C6-SH (m = 6, n = 38) and PAA-C9-SH (m = 9, n =7). Note, TFA is trifluoroacetic acid, and THF is tetrahydrofuran.

ATRP reaction is maintained under anoxic conditions at 50 °C for 24 hours and stopped by letting air into the flask. The copper catalyst is removed by passing the mixture through a basic alumina column. After solvent evaporation, the product $[\mathrm{PtBA{-}R{-}S}]_2$ is dissolved in a mixture of trifluoroacetic acid (8 mL) and tetrahydrofuran (2 mL) for the acidolysis of PtBA into PAA. The mixture is then stirred overnight and the solvent is evaporated to obtain the powdered product $[\mathrm{PAA{-}R{-}S}]_2$. The reaction products in each step are characterized by ^{1}H NMR spectroscopy, with deuterated chloroform or water as tsolvents. Molecular weight and polydispersity index (PDI) of the as-synthesized $[\mathrm{PtBA{-}R{-}S}]_2$ are estimated by gel permeation chromatography (GPC). The NMR and GPC results are provided in the Supporting Information (SI). The number averaged molecular masses M_n of the as-synthesized $[\mathrm{PAA{-}R{-}S}]_2$ are 6100 Da (38 AA units, PDI = 1.2) and 1630 Da (7 AA units, PDI = 1.08) for R=$-(\mathrm{CH_2})_6-$ and $-(\mathrm{CH_2})_9-$, respectively. More details are provided in the SI.

Capping AuNPs with PAA: AuNPs are functionalized with PAA using a protocol that is slightly modified from the documented procedures for functionalizating AuNPs with single-stranded DNA.[22,39,50] The PAA disulfide $[\text{PAA}-\text{R}-\text{S}]_2$ powder is dissolved in water and then buffered with a phosphate buffer (100 mM phosphate, pH 8.0). The disulfide bond is cleaved by the TCEP reducing gel by incubation for 1 hour. The freshly cleaved PAA−R−SH are mixed with citrate-stabilized AuNPs in a PAA−R−SH/AuNP molar ratio of $\sim 500/1$ to ensure maximum grafting density. The mixture is incubated under shaking at room temperature for about half a day. In the salting process, another phosphate buffer (10 mM phosphate, 3.0 M NaCl, pH 7.0) is gradually added to the mixture to elevate the NaCl concentration stepwise from 0 to 0.5 M over 7 steps within 2 days. In each step, half a minute of sonication is performed. The as-prepared PAA-capped AuNPs were purified by centrifugation (at $20000g \times 1$h), removing supernatant and resuspending pellets in Millipore water. The washing process is repeated at least three times to remove excess unbound PAA. The final concentration of PAA-AuNPs is determined by UV-Visible absorption. The actual mean size and size distribution of the AuNPs have also been determined by small-angle X-ray scattering (SAXS) measurements (See Fig. S5).[42,46] Our dynamic light scattering (DLS) measurements (see SI) show that the hydrodynamic diameter of the capped PAA-AuNP is ≈ 27 nm. Based on the DLS results, our theoretical model of the hydrodynamic size of polymer-capped NPs,[46,51] and the characteristics of PAA reported elsewhere,[52] the grafting density of PAA on AuNPs is estimated to be $\sigma = 0.30$ nm^{-2}, corresponding to $n = \sigma\pi D^2 = 73$ chains per particle (See SI). We note that the grafting number of thiolated-ssDNA for 10 nm AuNPs is reported to be 40–60 chains per particle.[40,41] Furthermore, the zeta-potential of the as-purchaed AuNPs is -37 mV compared to the capped particles at -31 mV.

To induce PAA-AuNPs migration and subsequent assembly at the liquid (suspension) surface, the pH level is manipulated using HCl solution. The pH values were changed by adding highly concentrated HCl step by step to the same sample in the trough, so that

the change in PAA-AuNPs concentration is negligible. In order to study the effect of salts at neutral pH, we use $MgCl_2$ salt with stock concentrations (0.01–2.2 M) to be added to the PAA-AuNP suspensions to get desired final concentrations of salts (typically 0.05–250 mM $MgCl_2$). We note that PAA-AuNPs start to form precipitates at the bottom of the trough at pH ≤ 2.2 or $[MgCl_2] \geq 50$ mM. In a separate set of experiments, we use a DPTAP Langmuir monolayer to attract the PAA-AuNPs to the positively charged template formed by the headgroups of DPTAP. As-purchased DPTAP is dissolved in 3:1 chloroform/methanol solution and then deposited on the liquid surface to obtain a positively-charged Langmuir monolayer.[42]

X-ray Scattering Setup

Synchrotron-based surface sensitive X-ray scattering techniques, i.e., grazing incidence small-angle X-ray scattering (GISAXS) and specular X-ray reflectivity (XRR), are used to monitor the interfacial self-assembly of PAA-AuNPs. The scattering experiments were conducted on the liquid surface spectrometer (LSS) at beamline 9 ID-B, Advanced Photon Source (APS), Argonne National Laboratory. The experimental details on the liquid surface scattering setup can be found elsewhere.[39,42,46] Briefly, aqueous suspension of PAA-AuNPs contained in a home-built trough is enclosed in a sealed chamber that is purged with water-saturated helium. The liquid surface is illuminated with a monochromatic X-ray beam (photon energy of $E = 8.0$ keV, wavelength $\lambda = 1.5497$ Å, wavevector $k_0 = 4.0545$ Å^{-1}) at an incident angle $\alpha_{\rm i}$ with the exit angle of $\alpha_{\rm f}$ (with respect to the surface). For the scattering vector $\mathbf{Q} = (Q_x, Q_y, Q_z)$, $Q_z = k_0(\sin\alpha_{\rm i} + \sin\alpha_{\rm f})$ along the surface normal, $Q_y = k_0 \cos\alpha_{\rm f} \sin\Psi$ (Ψ being the in-plane scattering angle) parallel to the liquid surface and perpendicular to the scattering plane, and $Q_x = k_0(\cos\alpha_{\rm f}\cos\Psi - \cos\alpha_{\rm i})$ normal to Q_y and Q_z and $Q_x \approx 0$ in this study. A 2D Pilatus 100K detector (487 × 195 pixels, 172 × 172 μm^2 per pixel) is used to collect the GISAXS maps as functions of of $Q_{xy} = (Q_x^2 + Q_y^2)^{1/2}$ and Q_z, while the reflectivity R as a function of $Q_z = 2k_0 \sin\alpha_{\rm i}$ is recorded by a Bicron point detector. The measured

reflectivity, R, is further normalized to the Fresnel reflectivity, R_F that is calculated for the ideally flat and smooth vapor–subphase interfaces. The electron density (ED) profiles along surface normal direction (ρ as a function of depth z) is extracted from the XRR through quantitative analyses using the effective-density model to construct ED profiles,[53] and the Prarratt's recursive method for data fitting.[54–56]

Results and Discussion

I. pH induced interfacial assembly and ordering

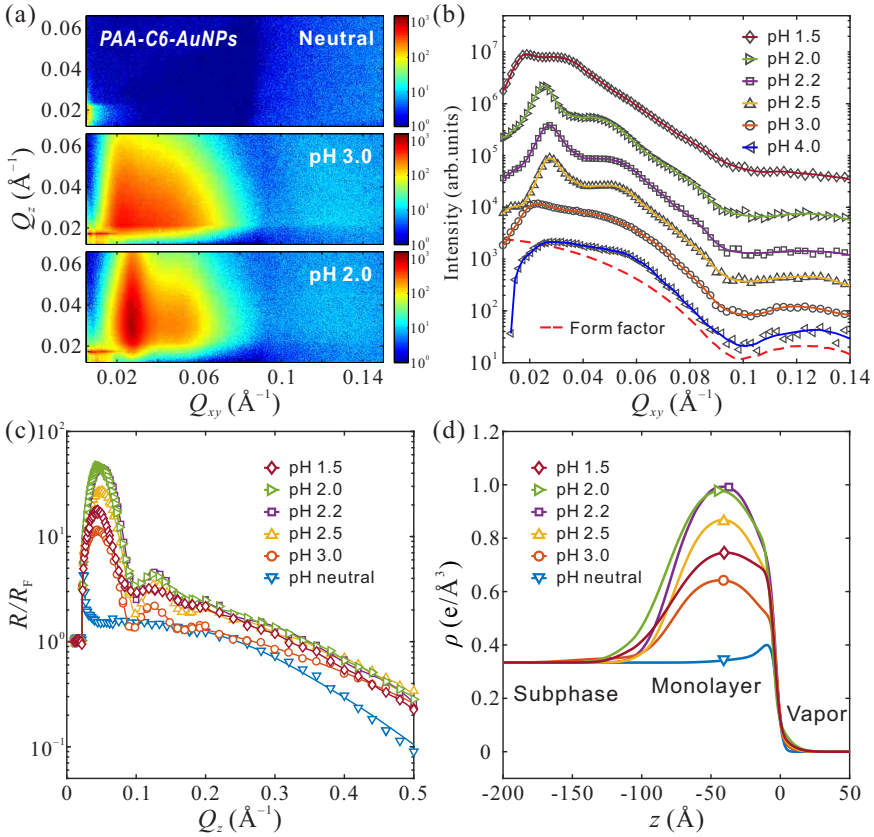

Figure 3: pH-induced self-assembly of PAA-C6-AuNPs at the vapor–liquid interfaces. (a) Representative GISAXS patterns as functions of Q_{xy} and Q_z for aqueous suspensions of PAA-C6-AuNPs at neutral pH and other pH values as indicated. A detailed evolution is shown in Fig. S7. Intensities are displayed on logarithmic scales. (b) Horizontal linecut profiles from GISAXS patterns along Q_{xy} direction at $Q_z = 0.020$ Å^{-1} integrated over Q_z range 8.5 $\times 10^{-3}$ Å^{-1} in the low Q_{xy} range (0.02–0.14 Å^{-1}). Also shown is a form factor profile (dase line) measured by SAXS from the PAA-C6-AuNPs dispersed in water at neutral pH. The plots are vertically shifted for clarity. Solid lines are guides to the eyes. (c) Representative normalized XRR data R/R_F for aqueous suspensions of PAA-C6-AuNPs under the same experimental conditions as the GISAXS measurements. (d) Representative best-fit electron density profiles along surface normal direction that regenerate R/R_F (solid lines) in (c).

Figure 3 showing GISAXS and XRR measurements conveys the main features of the structural evolution of self-assembly and crystallization of PAA-C6-AuNPs at the vapor–liquid interface at neutral pH and pH = 1.5 to 4.0. Figure 3a and Fig. S7 (in the SI) show (Q_{xy}, Q_z) GISAXS maps at various pH values, and Figure 3b displays line-cuts along the Q_{xy} direction at $Q_z = 0.020$ Å^{-1} integrated over Q_z range 8.5 $\times 10^{-3}$ Å^{-1}. At neutral pH, the GISAXS shows a pattern void of any features, evidence of insignificant amount or no nanoparticles at the interface. However, at pH = 4.0, the GISAXS pattern shows a broad feature for which the line-cut is dominated by a form factor that corresponds to AuNPs. This demonstrates that the PAA-C6-AuNPs spontaneously migrate to the interface and form a Gibbs monolayer of almost uncorrelated particles.

Lowering the pH further (below 3) gives rise to a broad pattern indicating crystallization of the Gibbs monolayer. The GISAXS linecut profiles display a combination of the form factor and the structure factor of the surface-adsorbed AuNPs. Particularly, at pH = 2.0–2.5, well-defined fundamental diffraction peaks emerge at $Q_1 \approx 0.025 - 0.028$ Å^{-1}. In Fig. S8, the extracted structure factor $S(Q_{xy})$ shows that the relative peak positions with respect to the fundamental diffraction peaks are $Q_i/Q_1 \approx 1 : 2 : 3$ ($i = 1, 2, 3$). This pattern is consistent with short-range order of one-dimensional (1D) string-like phase, where the surface-adsorbed particles are aligned into a chain-like structure with the inter-particle spacing of $d_L = 2\pi/Q_1$ ($d_L = 22$–25 nm for pH = 2.5–2.0). When the pH value is decreased to 1.5, the Gibbs monolayer appears to be less ordered, as the interfacial assemblies are no longer stable and form precipitates.

The XRR measurements (Fig. 3c) of the same samples show similar results of Gibbs monolayer formation at the interface as pH values are lowered. Whereas the XRR at neutral pH falls off monotonically with increasing Q_z, strong oscillations with high amplitude are apparent in the low Q_z region ($Q_z \leq 0.2$ Å^{-1}) as the pH decreases, indicating the formation of a high electron density (ED) film at the interface. As shown in Fig. 3d, the extracted ED profiles, from the best fit to the XRR, exhibit a significant increase of ED with a ∼10

nm thick film. In view of the fact that the ED of PAA-C6-AuNPs is dominated by Au cores of sizes of 8.8 ± 0.9 nm in diameter (as measured by SAXS; Fig. S5) we conclude that PAA-C6-AuNPs self-assemble into a mono-particle layer at low pH levels, and note that the maxima of the ED gradually increase from neutral pH to pH = 2.0–2.2 owing to the interfacial accumulation (i.e. higher in-plane densities), and drop at pH = 1.5 due to precipitation, which is consistent with the GISAXS results.

The pH-dependent interfacial accumulation and ordering of PAA-C6-AuNPs is attributed to the hydrophobic/hydrophilic character of alkyl-PAA ligands in aqueous solutions. Adjusting the pH level affects the dissociation equilibria of carboxyl groups, leading to gradual dominance of the hydrophobic alkyl chains of PAA-capped AuNPs that cause their migration to the interface. The effect of the hydrocarbons is not sufficient to overcome the PAA affinity to water at neutral pH. However, lowering the pH, below roughly the pKa of the carboxyl groups (for PAA the pKa $\sim$ 4.5[59]) reduces the PAA affinity to water and gives way to the hydrophobic effect by hydrocarbons to dominate and push the capped NPs to the surface. At neutral pH the majority of carboxyl groups remain charged and the PAA-AuNPs bear electrostatic repulsion, while $\geq$ 97 % of carboxyl groups become protonated at pH $\leq$ 3, reducing water-affinity and promoting hydrogen-bonding between the neighboring PAA-AuNPs[59] due to the large number of PAA-AuNPs present at the interface. We note that at low pH hydrogen bonds formed between the protonated carboxyl groups facilitate interparticle interactions and robust ordering.[57,58] Reduction in ssDNA affinity to water by adding salts to DNA-capped AuNPs suspensions and hydrophobic effects (due hydrocarbon segments of the functionalized ssDNA) similarly explain the formation and crystallization of these DNA-AuNPs at liquid-vapor interface.[39] The formed chain-like structure of linked particles is similar to the branched assembly of carboxylates-capped nanoparticles on solid substrates.[60] Although non-specific, the attraction of PAA through hydrogen-bonding is analogous to the hybridization of complementary ssDNA through base-pairing,[61] thus, also consistent with the chain-like results on the base-pairing of complementary ssDNA-capped

AuNPs on liquid surfaces.[40] Interestingly, the Gibbs monolayers of PAA-AuNPs consistently maintain a single-particle layer even though crosslinked by hydrogen-bonding, while the complementary ssDNA-AuNPs form roughly a two-layer film at the interface.[39] Based on the ED extracted from the XRR and average interparticle distance (as illustrated in Fig. 4) assuming various close-packing (square and hexagonal lattices, and including AuNPs size distributions) we estimate the surface coverage of the PAA-AuNP ordered assemblies to be at $95 - 100\%$ (see more details on calculating the estimated coverage in the SI of Ref. [46]; here, *surface coverage* should not be confused with the hexagonal packing-density of spheres or discs in a plane).

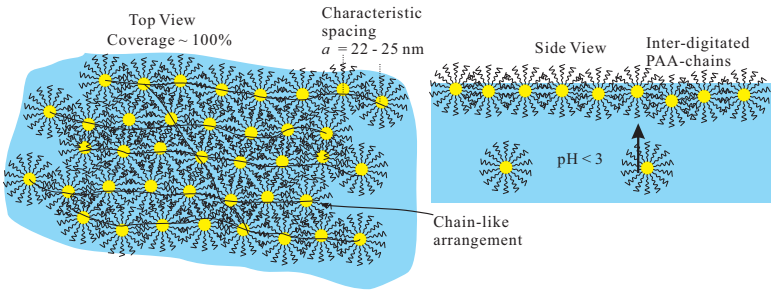

Figure 4: Illustration of the arrangement of PAA-AuNPs at the vapor/solution interface after adjusting the pH to below 3. Based on the GISAXS and the ED extracted from the XRR we estimate the coverage of the short-range-crystalline Gibbs monolayer to be close to 100%

II. Assembly induced by $MgCl_2$

The effect of $MgCl_2$ concentrations on the interfacial self-assembly of PAA-AuNPs is described below. Figure 5a-b and Fig. S10 display the in-plane structural evolution of PAA-C6-AuNPs at the vapor–liquid interface at various $MgCl_2$ concentrations ($[MgCl_2] = 0$ and 0.05–250 mM). GISAXS patterns show that at low $[MgCl_2]$ (≤ 0.05 mM), almost all of the PAA-C6-AuNPs are dispersed in the bulk solution. When the $[MgCl_2]$ is ≥ 0.5 mM, some PAA-C6-AuNPs spontaneously accumulate at the interface and give rise to well-defined form factors and to finite structural correlations. The interfacial self-assembly of PAA-C6-AuNPs mediated by $MgCl_2$ is somewhat consistent with previous studies on the ssDNA-capped AuNPs,[39] as PAA-C6-AuNP assemblies reveal different structural transitions. At interme-

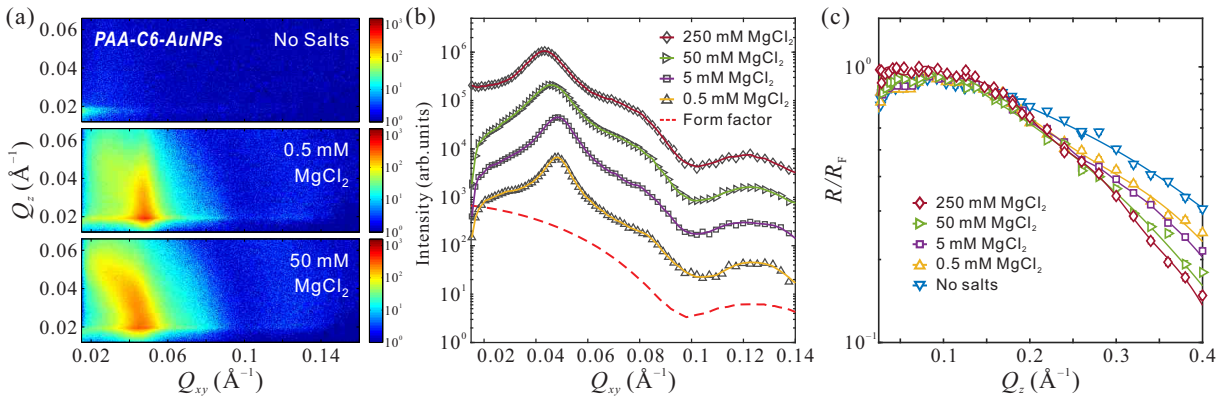

Figure 5: $MgCl_2$ induced self-assembly of PAA-C6-AuNPs at the vapor–liquid interfaces. (a) Representative GISAXS patterns as functions of Q_{xy} and Q_z for aqueous suspensions of PAA-C6-AuNPs in the absence of salts and in the presence of $MgCl_2$ at various concentrations as indicated. A detailed evolution is shown in Fig. S10. Intensities are displayed on logarithmic scales. (b) Horizontal linecut profiles from GISAXS patterns along Q_{xy} direction at $Q_z = 0.020$ Å^{-1} integrated over Q_z range 8.5 $\times 10^{-3}$ Å^{-1} at low Q_{xy} range (0.02–0.14 Å^{-1}). Also shown is a form factor profile (dash line) measured by SAXS from the PAA-C6-AuNPs dispersed in water without any salts. The plots are vertically shifted for clarity. (c) Representative normalized XRR data R/R_{F} for aqueous solutions suspensions of PAA-C6-AuNPs under experimental the same conditions as the GISAXS measurements. Solid lines in (b) and (c) are guides to the eyes.

diate levels of $MgCl_2$ (0.5 mM), the Bragg diffraction rod suggests that 2D structures set in, and transform to 3D phases at high [$MgCl_2$] (5–50 mM), as evidenced by the fading-away of the Bragg rod and the emergence of ring-like diffraction (arcs) patterns at almost the same Q_{xy} positions shown in the GISAXS patterns (Fig. S10). The fundamental diffraction peaks at $Q_1 \approx 0.043 - 0.048$ Å^{-1} indicate a characteristic inter-particle distance of $a_L = 2\pi/Q_1 =$ 13–15 nm, which is much smaller than the inter-particle spacing (22–25 nm) in the assemblies of the same PAA-AuNPs induced by low pH. We note that the synthesized PAA-C6 in this study has an average molecular weight of 3 kDa and as such it is rigid and it tends to remain in extended conformation regardless of pH because of limited chain length.[59] By contrast, owing to the strong chemical association between multivalent cations and carboxyl groups, the addition of $MgCl_2$ causes inter-crosslinked chains of neighboring particles (i.e., interdigitation) and crosslinking between neighboring PAA chains on the same particles.[63] This may explain the much shorter interparticle distance in $MgCl_2$-induced assemblies compared to that induced by lowering the pH.

The XRR results of the same samples are shown in Fig 5c. With the increase of [$MgCl_2$] from 0 to 250 mM, significant decay of the XRR at high Q_z is observed, suggesting higher surface roughness. However, the overall XRR curves are smooth without clear oscillations.

This indicates that the liquid surface is only partially covered by the adsorbed assembled AuNPs. Based on the additivity property, the total reflectivity $R_{\text{tot}} = \alpha R_{\text{ml}} + (1-\alpha)R_{\text{w}}$, where R_{ml} and R_{w} are reflectivity from the nanoparticle monolayer on the aqueous surface and the pure water surface, respectively, and α is the surface coverage of the nanoparticle monolayer. Here, because of the low α, the non-uniform surface is dominated by the bare solution surface, although sparse floating islands of PAA-C6-AuNP clusters with short-range ordering are present. Therefore, the XRR from PAA-C6-AuNP solution mixed with $MgCl_2$ can practically be considered as a reflectivity of a water-solution surface with an emergent increase of roughness due to the absorption of AuNP clusters. Compared to the pH-induced assemblies with distinct mono-particle layers presented above, the effect of $MgCl_2$ on the interfacial accumulation is less pronounced (as illustrated in the SI).

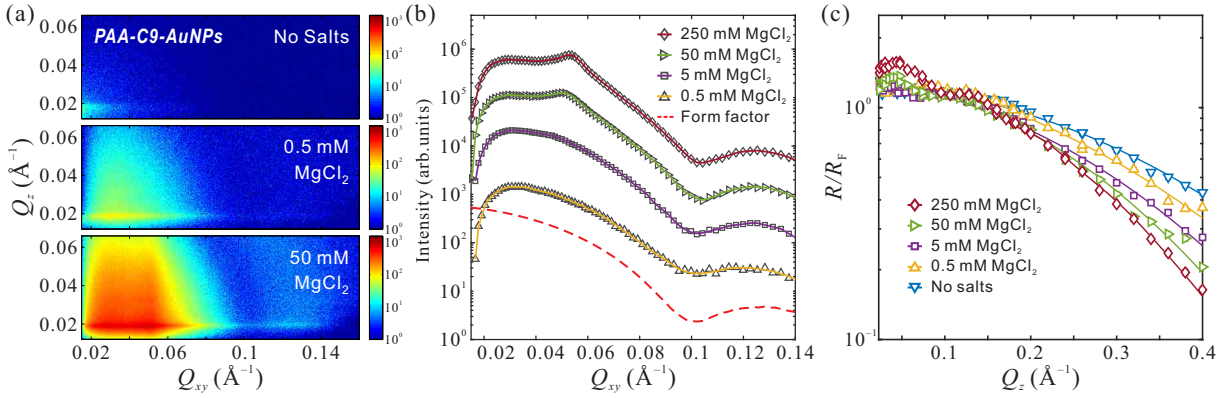

Figure 6: $MgCl_2$ induced self-assembly of PAA-C9-AuNPs at the vapor–liquid interfaces. (a) Representative GISAXS patterns as functions of Q_{xy} and Q_z for aqueous suspensions of PAA-C9-AuNPs in the absence of salts and in the presence of $MgCl_2$ at various concentrations as indicated. A detailed evolution is shown in Fig. S11. Intensities are displayed on logarithmic scales. (b) Horizontal linecut profiles from GISAXS patterns along Q_{xy} direction at $Q_z = 0.020$ Å^{-1} integrated over Q_z range 8.5 $\times 10^{-3}$ Å^{-1} at low Q_{xy} range (0.02–0.14 Å^{-1}). Also shown is a form factor profile measured by SAXS from the PAA-C9-AuNPs dispersed in water without any salts. The plots are vertically shifted for clarity. (c) Representative normalized XRR data R/R_{F} for aqueous solutions suspensions of PAA-C9-AuNPs under experimental the same conditions as the GISAXS measurements. Solid lines in (b) and (c) are guides to the eyes.

To improve the ability of PAA-capped AuNPs to migrate to the interface, another type of alkyl-PAA ligands (PAA-C9), with shorter PAA segments and longer hydrocarbons than those of PAA-C6, is examined. The evolution of the in-plane and surface-normal structures of PAA-C9-AuNPs at the interface are shown in Fig. 6 and Fig. S11 and similar to PAA-C6-AuNPs adsorb to the liquid surface at about the same $[MgCl_2] \geq 0.5$ mM, however, with strong signs of ordering at this concentration. Short-range order appears only at a threshold

concentration of [$MgCl_2$] $\approx$ 50 mM with a primary diffraction peak at $Q_1 \approx 0.051 - 0.053$ Å^{-1} corresponding $a_L \approx 12$ nm. The a_L is slightly smaller than that of the PAA-C6-AuNP assemblies as the PAA-C9 is shorter than the PAA-C6. Furthermore, additional weak oscillations emerge in low Q_z region of the XRR data for PAA-C9-AuNPs at high [$MgCl_2$] ($\geq$50 mM), suggesting that the interface is more populated with nanoparticles than that of PAA-C6-AuNPs (Fig. S12). Nevertheless, just like for PAA-C6 the surface of PAA-C9-AuNPs is only partially covered with assembled NPs. We argue that the overall hydrophobicity of $MgCl_2$-neutralized PAA-C9-AuNPs is higher than that of PAA-C6-AuNPs, thus more PAA-C9-AuNPs accumulate at the interface and have a higher chance to form a complete Gibbs monolayer. Owing to longer PAA chains, PAA-C6-AuNPs probably have inter-particle interactions through the binding of divalent ions Mg^{2+}, even before the nanoparticles migrate to the interfaces. By contrast, it is more likely that PAA-C9-AuNPs adsorb at the interfaces as individual particles without inter-particle interactions due to the quite short PAA ligands.

III. Positively charged template-induced assembly and ordering

Figure 7 shows the GISAXS and XRR results of DPTAP lipids spread on PAA-C6-AuNPs at various pH levels. DPTAP itself forms stable cationic Langmuir monolayers on aqueous surface as shown in the XRR and ED profile, similar to results in the literature.[42,62] The presence of DPTAP monolayers facilitates accumulation of PAA-AuNPs at the interface through electrostatic interactions. At neutral pH, the 2D GISAXS pattern from DPTAP with PAA-AuNPs (Fig. 7a) shows strong scattering from AuNPs in spite of being less ordered, which is distinct from the featureless pattern from PAA-AuNP suphase alone (Fig. 3a). Meanwhile, the XRR (Fig. S9) confirms the existence of a mono-particle layer (with thickness of $\sim$10 nm) beneath the DPTAP monolayer. Recently, the DPTAP has been used to attract negatively-charged ssDNA-capped or citrated-stabilized AuNPs to form 2D nanoparticle assemblies.[40–42] Here, we show that the PAA-AuNPs can be also assembled using oppositely-charged Langmuir templates at a liquid surface, which bears a resemblance

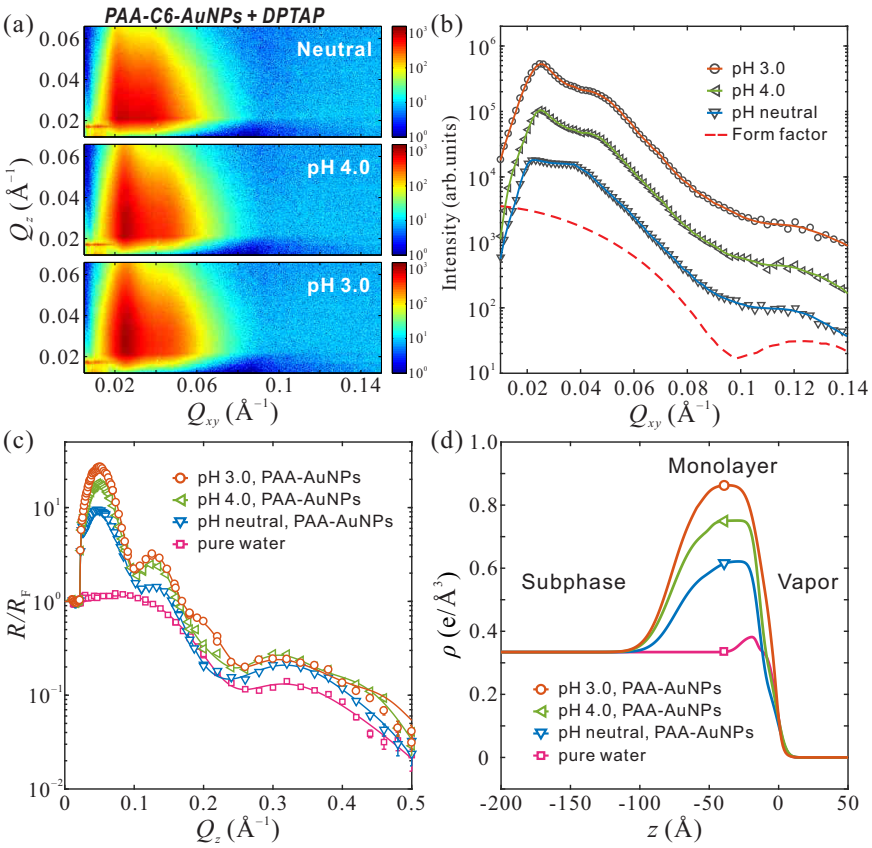

Figure 7: Self-assembly of PAA-C6-AuNPs at the charged membrane (DPTAP) interfaces. (a) Representative GISAXS patterns as functions of Q_{xy} and Q_z for DPTAP monolayers spread on the aqueous subphases of PAA-C6-AuNPs at neutral pH and various pH values as indicated. Intensities are displayed on logarithmic scales. (b) Horizontal linecut profiles from GISAXS patterns in (a) along Q_{xy} direction at $Q_z = 0.020$ Å^{-1} integrated over Q_z range 8.5 $\times 10^{-3}$ Å^{-1} at low Q_{xy} range (0.02–0.14 Å^{-1}). Also shown is a form factor profile (dase line) measured by SAXS from the PAA-C6-AuNPs dispersed in water at neutral pH. The plots are vertically shifted for clarity. Solid lines are guides to the eyes. (c) Representative normalized XRR data R/R_{F} for DPTAP monolayers spread on pure water subphase and aqueous subphases containing PAA-C6-AuNPs under the same experimental conditions as the GISAXS measurements. (d) Representative best-fit electron density profiles along surface normal direction that regenerate R/R_{F} (solid lines) in (c).

to assembly of DNA-capped nanoparticles. Furthermore, by lowering the pH of the PAA-C6-AuNP subphase in the presence of DPTAP, more particles are adsorbed to the interface as the intensities of first maxima in XRR and the corresponding ED are increased, as depicted in Fig. 8. The GISAXS results suggest that the ordering of PAA-AuNPs is improved ($Q_1 \approx 0.025$ Å^{-1}) with decreased pH. Although at low pH the protonation of carboxyl groups reduces the charge of PAA-AuNPs, it strengthens significantly the positive charge of the DPTAP and attracts more particles at the interface. Moreover, the increased hydrophobicity as discussed above also contributes to interfacial accumulation of PAA-AuNPs. The XRR (Fig. 7c) shows that, similar to the pH induced Gibbs monolayers, the 2D particle assemblies templated by DPTAP form a mono-particle layer (Fig. 7d).

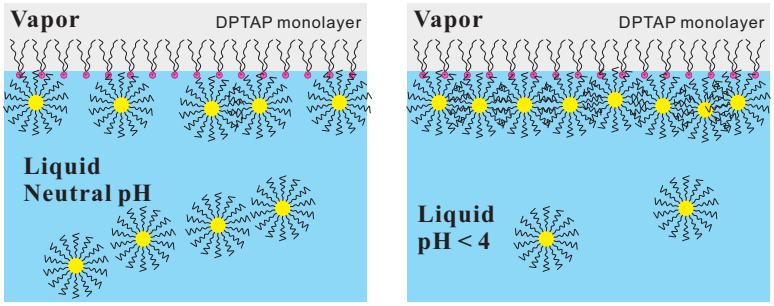

Figure 8: Depiction of the positively charged surface achieved by forming a DPTAP Langmuir monolayer at the liquid vapor interface. At neutral pH the capped PAA-AuNPs adhere to the charged interface however at lower density compared to a suspension at pH values smaller than 4.

Conclusion

By functionalizing synthetic polyelectrolytes, alkylthiol-terminated PAA, and grafting them on AuNPs, we demonstrate similarities in their interfacial assembly to those of ssDNA-AuNPs. Employing GISAXS and XRR, we show that PAA-AuNPs in aqueous suspension spontaneously accumulate at the vapor–liquid interface and form a Gibbs monolayer by tuning pH levels or salt concentrations. The formation of a Gibbs monoalyer is induced by the overall hydrophobicity of PAA-AuNPs by lowering the affinity of PAA to water molecules and controlling the hydrophobic effect by manipulating the length of the alkylthiol attached to the

PAA. By adjusting pH, the in-plane ordering at the interface is 1D chain-like structure, likely driven by strong hydrogen bonds among neighboring PAAs. The interfacial self-assembly of PAA-AuNPs can also be mediated by introducing salts to the subphase, i.e., $MgCl_2$. Owing to the strong associations between Mg^{2+} and COO^- groups, PAA-AuNPs form 2D clusters with short-range order, which further transform to 3D structures that precipitate. Therefore, the interfacial accumulation induced by salts is less pronounced than that achieved by lowering the pH. Low pH levels can lead to hydrogen-bonds that render intermediate and reversible binding strengths suitable as knobs to fine-tune interactions among nanoparticles (not tested in this study). We also show that, by analogy to the assembling of DNA-AuNPs at charged interfaces, that PAA-AuNPs assemble at a positively charged Langmuir monolayer that is formed by DPTAP by virtue of electrostatic interactions. In fact, fluid-fluid interfaces, such as the water/oil have been extensively used to self-assemble of charged nanoparticles[19,64] demonstrating an arrangement tunability[65] and reversible partitioning.[66] Our findings point to the potential of using polyelectrolytes to functionalize nanoparticles and taking advantage of tweaking hydrogen bonding to control their assemblies.

Associated Content

Supporting Information

The Supporting Information is available free of charge on the

ACS Publications website at DOI: 10.1021/acs.***.yyyyyy

Detailed synthesis and characterization of alkylthiol-terminated-PAA. SAXS measurements of uncapped AuNPs and PAA-AuNPs. pH- and MgCl2-induced interfacial assembly of PAA-AuNPs, including control experiments extraction of $S(Q_{xy})$, and XRR.

Acknowledgement

We thank Alex Travesset for useful discussions leading to this project, and Ivan Kuzmenko at beamline 9ID-B, APS, Argonne National Laboratory for technical support in liquid surface scattering measurements. We also acknowledge Xiaobing Zuo at beamline 12ID-B, APS, Argonne National Laboratory for technical support in measuring SAXS of nanoparticles in bulk solutions. We thank Ms. Grace Bjorland, Mr. Farhan Islam and Mr. Nicholas J Breslin for their experimental help at APS. Research was supported by the U.S. Department of Energy (U.S. DOE), Office of Basic Energy Sciences, Division of Materials Sciences and Engineering. Ames Laboratory is operated for the U.S. DOE by Iowa State University under Contract No. DE-AC02-07CH11358. Use of the Advanced Photon Source, an Office of Science User Facility operated for the U.S. DOE Office of Science by Argonne National Laboratory, was supported by the U.S. DOE under Contract No. DE-AC02-06CH11357.

References

(1) Decher, G. Fuzzy Nanoassemblies: Toward Layered Polymeric Multicomposites. *Science* **1997**, *277*, 1232-1237

(2) Caruso, F.; Caruso, R. A.; Möhwald, H. Nanoengineering of Inorganic and Hybrid Hollow Spheres by Colloidal Templating. *Science* **1998**, *282*, 1111-1114.

(3) Richardson, J. J.; Björnmalm, M.; Caruso, F. Technology-Driven Layer-by-Layer Assembly of Nanofilms. *Science* **2015**, *348*, aaa2491.

(4) Decher, G.; Schlenoff, J. B. *Multilayer Thin Films: Sequential Assembly of Nanocomposite Materials*. Wiley: 2012.

(5) Hiller, J. A.; Mendelsohn, J. D.; Rubner, M. F. Reversibly Erasable Nanoporous Anti-Reflection Coatings from Polyelectrolyte Multilayers. *Nat. Mater.* **2002**, *1*, 59-63.

(6) Mei, Y.; Lu, Y.; Polzer, F.; Ballauff, M.; Drechsler, M. Catalytic Activity of Palladium Nanoparticles Encapsulated in Spherical Polyelectrolyte Brushes and Core–Shell Microgels. *Chem. Mater.* **2007**, *19*, 1062-1069.

(7) Hamedi, M.; Karabulut, E.; Marais, A.; Herland, A.; Nyström, G.; Wågberg, L. Nanocellulose Aerogels Functionalized by Rapid Layer-by-Layer Assembly for High Charge Storage and Beyond. *Angew. Chem., Int. Ed.* **2013**, *52*, 12038-12042.

(8) Thierry, B.; Winnik, F. M.; Merhi, Y.; Tabrizian, M. Nanocoatings onto Arteries via Layer-by-Layer Deposition: Toward the in Vivo Repair of Damaged Blood Vessels. *J. Am. Chem. Soc* **2003**, *125*, 7494-7495.

(9) Wilson, J. T.; Cui, W.; Kozlovskaya, V.; Kharlampieva, E.; Pan, D.; Qu, Z.; Krishnamurthy, V. R.; Mets, J.; Kumar, V.; Wen, J.; Song, Y.; Tsukruk, V. V.; Chaikof, E. L. Cell Surface Engineering with Polyelectrolyte Multilayer Thin Films. *J. Am. Chem. Soc* **2011**, *133*, 7054-7064.

(10) Decher, G.; Hong, J. D.; Schmitt, J. Buildup of Ultrathin Multilayer Films by a Self-Assembly Process: III. Consecutively Alternating Adsorption of Anionic and Cationic Polyelectrolytes on Charged Surfaces. *Thin Solid Films* **1992**, *210*, 831-835.

(11) Gittins, D. I.; Caruso, F. Multilayered Polymer Nanocapsules Derived from Gold Nanoparticle Templates. *Adv. Mater.* **2000**, *12*, 1947-1949.

(12) Schneider, G.; Decher, G. From Functional Core/Shell Nanoparticles Prepared via Layer-by-Layer Deposition to Empty Nanospheres. *Nano Lett.* **2004**, *4*, 1833-1839.

(13) Collier, C. P.; Saykally, R. J.; Shiang, J. J.; Henrichs, S. E.; Heath, J. R. Reversible tuning of silver quantum dot monolayers through the metal-insulator transition. *Science*, **1997**, *277*, 1978-1981.

(14) Lin, Y.; Skaff, H.; Emrick, T.; Dinsmore, A. D.; Russell, T. P. Nanoparticle Assembly and Transport at Liquid-Liquid Interfaces. *Science* , **2003**, *299*, 226-229.

(15) Li, J. J.; Wang, Y. A.; Guo, W. Z.; Keay, J. C.; Mishima, T. D.; Johnson, M. B.; Peng, X. G., Large-scale synthesis of nearly monodisperse CdSe/CdS core/shell nanocrystals using air-stable reagents via successive ion layer adsorption and reaction. *Journal of the American Chemical Society*, **2003**, *125*, 12567-12575.

(16) Tao, A.; Sinsermsuksakul, P.; Yang, P. Tunable plasmonic lattices of silver nanocrystals. *Nature Nanotechnology*, **2007**, *2*, 435-440.

(17) Martinez, A. C.; Rio, E.; Delon, G.; Saint-Jalmes, A.; Langevin, D.; Binks, B. P. On the origin of the remarkable stability of aqueous foams stabilised by nanoparticles: link with microscopic surface properties. *Soft Matter*, **2008**, *4*, 1531-1535.

(18) Cheng, L.; Liu, A.; Peng, S.; Duan, H. Responsive Plasmonic Assemblies of Amphiphilic Nanocrystals at Oil-Water Interfaces. *Acs Nano*, **2010**, *4*, 6098-6104.

(19) Garbin, V.; Crocker, J. C.; Stebe, K. J. Nanoparticles at fluid interfaces: Exploiting capping ligands to control adsorption, stability and dynamics. *Journal of Colloid and Interface Science*, **2012**, *387*, 1-11. (and references therein).

(20) Mirkin, C. A.; Letsinger, R. L.; Mucic, R. C.; Storhoff, J. J. A DNA-Based Method for Rationally Assembling Nanoparticles into Macroscopic Materials. *Nature* **1996**, *382*, 607-609.

(21) Alivisatos, A. P.; Johnsson, K. P.; Peng, X.; Wilson, T. E.; Loweth, C. J.; Bruchez, M. P.; Schultz, P. G. Organization of 'Nanocrystal Molecules' Using DNA. *Nature* **1996**, *382*, 609-611.

(22) Maye, M. M.; Nykypanchuk, D.; van der Lelie, D.; Gang, O. A Simple Method for

Kinetic Control of DNA-Induced Nanoparticle Assembly. *J. Am. Chem. Soc.* **2006**, *128*, 14020-14021.

(23) Shenton, W.; Davis, S. A.; Mann, S. Directed Self-Assembly of Nanoparticles into Macroscopic Materials Using Antibody/Antigen Recognition. *Adv. Mater.* **1999**, *11*, 449-452.

(24) McMillan, R. A.; Paavola, C. D.; Howard, J.; Chan, S. L.; Zaluzec, N. J.; Trent, J. D. Ordered Nanoparticle Arrays Formed on Engineered Chaperonin Protein Templates. *Nat. Mater.* **2002**, *1*, 247-252.

(25) Sun, J.; DuFort, C.; Daniel, M.-C.; Murali, A.; Chen, C.; Gopinath, K.; Stein, B.; De, M.; Rotello, V. M.; Holzenburg, A.; Kao, C. C.; Dragnea, B. Core-Controlled Polymorphism in Virus-Like Particles. *Proc. Natl. Acad. Sci. U.S.A.* **2007**, *104*, 1354-1359.

(26) Nykypanchuk, D.; Maye, M. M.; van der Lelie, D.; Gang, O. DNA-Guided Crystallization of Colloidal Nanoparticles. *Nature* **2008**, *451*, 549-552.

(27) Park, S. Y.; Lytton-Jean, A. K. R.; Lee, B.; Weigand, S.; Schatz, G. C.; Mirkin, C. A. DNA-Programmable Nanoparticle Crystallization. *Nature* **2008**, *451*, 553-556.

(28) Cheng, W.; Campolongo, M. J.; Cha, J. J.; Tan, S. J.; Umbach, C. C.; Muller, D. A.; Luo, D. Free-Standing Nanoparticle Superlattice Sheets Controlled by DNA. *Nat. Mater.* **2009**, *8*, 519-525.

(29) Jones, M. R.; Macfarlane, R. J.; Lee, B.; Zhang, J.; Young, K. L.; Senesi, A. J.; Mirkin, C. A. DNA-Nanoparticle Superlattices Formed from Anisotropic Building Blocks. *Nat. Mater.* **2010**, *9*, 913-917.

(30) Macfarlane, R. J.; Lee, B.; Jones, M. R.; Harris, N.; Schatz,G. C.; Mirkin, C. A. Nanoparticle Superlattice Engineering with DNA. *Science* **2011**, *334*, 204-208.

(31) Zhang, Y.; Lu, F.; Yager, K. G.; van der Lelie, D.; Gang, O. A general Strategy for the DNA-Mediated Self-Assembly of Functional Nanoparticles into Heterogeneous Systems. *Nat. Nanotechnol.* **2013**, *8*, 865-872.

(32) Macfarlane, R. J.; Thaner, R. V.; Brown, K. A.; Zhang, J.; Lee, B.; Nguyen, S. T.; Mirkin, C. A. Importance of the DNA"Bond" in pProgrammable Nanoparticle Crystallization. *Proc. Natl. Acad. Sci. U.S.A.* **2014**, *111*, 14995-15000.

(33) Tian, Y.; Wang, T.; Liu, W.; Xin, H. L.; Li, H.; Ke, Y.; Shih, W. M.; Gang, O. Prescribed Nanoparticle Cluster Architectures and Low-Dimensional Arrays Built Using Octahedral DNA Origami Frames. *Nat. Nanotechnol.* **2015**, *10*, 637-644.

(34) Liu, W.; Halverson, J.; Tian, Y.; Tkachenko, A. V.; Gang, O. Self-Organized Architectures from Assorted DNA-Framed Nanoparticles. *Nat. Chem.* **2016**, *8*, 867-873.

(35) Liu, W.; Tagawa, M.; Xin, H. L.; Wang, T.; Emamy, H.; Li, H.; Yager, K. G.; Starr, F. W.; Tkachenko, A. V.; Gang, O. Diamond Family of Nanoparticle Superlattices. *Science* **2016**, *351*, 582-586.

(36) Tian, Y.; Zhang, Y.; Wang, T.; Xin, H. L.; Li, H.; Gang, O. Lattice Engineering Through Nanoparticle-DNA Frameworks. *Nat. Mater.* **2016**, *15*, 654-661.

(37) Campolongo, M. J.; Tan, S. J.; Smilgies, D. M.; Zhao, M.; Chen, Y.; Xhangolli, I.; Cheng, W. L.; Luo, D. Crystalline Gibbs Monolayers of DNA-Capped Nanoparticles at the Air-Liquid Interface. *ACS Nano* **2011**, *5*, 7978-7985.

(38) Tan, S. J.; Kahn, J. S.; Derrien, T. L.; Campolongo, M. J.; Zhao, M.; Smilgies, D. M.; Luo, D. Crystallization of DNA-Capped Gold Nanoparticles in High-Concentration, Divalent Salt Environments. *Angew. Chem., Int. Ed.* **2014**, *53*, 1316-1319.

(39) Zhang, H.; Wang, W.; Hagen, N.; Kuzmenko, I.; Akinc, M.; Travesset, A.; Mallapra-

gada, S.; Vaknin, D. Self-Assembly of DNA Functionalized Gold Nanoparticles at the Liquid-Vapor Interface. *Adv. Mater. Interfaces* **2016**, *3*, 1600180.

(40) Srivastava, S.; Nykypanchuk, D.; Fukuto, M.; Halverson, J. D.; Tkachenko, A. V.; Yager, K. G.; Gang, O. Two Dimensional DNA-Programmable Assembly of Nanoparticles at Liquid Interfaces. *J. Am. Chem. Soc.* **2014**, *136*, 8323-8332.

(41) Srivastava, S.; Nykypanchuk, D.; Fukuto, M.; Gang, O. Tunable Nanoparticle Arrays at Charged Interfaces. *ACS Nano* **2014**, *8*, 9857-9866.

(42) Wang, W.; Zhang, H.; Kuzmenko, I.; Mallapragada, S.; Vaknin, D. Assembling Bare Au Nanoparticles at Positively Charged Templates. *Sci. Rep.* **2016**, *6*, 26462.

(43) Narayanan, S.; Wang, J.; Lin, X.-M. Dynamical Self-Assembly of Nanocrystal Superlattices during Colloidal Droplet Evaporation by *in situ* Small Angle X-Ray Scattering. *Phys. Rev. Lett.* **2004**, *93*, 135503/1-4.

(44) Bigioni, T. P.; Lin, X.-M.; Nguyen, T. T.; Corwin, E. I.; Witten, T. A.; Jaeger, H. M. Kinetically Driven Self Assembly of Highly Ordered Nanoparticle Monolayers. *Nat. Mater.* **2006**, *5*, 265-270.

(45) Geuchies, J. J.; van Overbeek, C.; Evers, W. H.; Goris, B.; de Backer, A.; Gantapara, A. P.; Rabouw, F. T.; Hilhorst, J.; Peters, J. L.; Konovalov, O.; Petukhov, A. V.; Dijkstra, M.; Siebbeles, L. D. A.; van Aert, S.; Bals, S.; Vanmaekelbergh, D. In-situ Study of the Formation Mechanism of Two-Dimensional Superlattices from PbSe Nanocrystals. *Nat. Mater.* **2016**, *15*, 1248-1254.

(46) Zhang, H.; Wang, W.; Mallapragada, S.; Travesset, A.; Vaknin, D. Macroscopic and Tunable Nanoparticle Superlattices. *Nanoscale* **2017**, *9*, 164-171.

(47) Zhang, H.; Wang, W.; Mallapragada, S. K.; Travesset, A.; Vaknin, D. Ion-Specific

Interfacial Crystallization of Polymer-Grafted Nanoparticles. *J. Phys. Chem. C* **2017**, *121*, 15424-15429.

(48) Shah, R. R.; Merreceyes, D.; Husemann, M.; Rees, I.; Abbott, N. L.; Hawker, C. J.; Hedrick, J. L. Using Atom Transfer Radical Polymerization to Amplify Monolayers of Initiators Patterned by Microcontact Printing into Polymer Brushes for Pattern Transfer. *Macromolecules* **2000**, *33*, 597-605.

(49) Kanapathipillai, M.; Rawal, A.; Yusufoglu, Y.; Hu, Y.-Y.; Lo, C.T.; Thiyagaraja, P.; Kalay, Y. E.; Akinc, M.,;Mallapragada, S.K.; Schmidt-Rohr, K. Ionic Block Copolymer Template Directed Calcium Phosphate Nanocomposites., *Chem. Mater.,* **2008**, *20*, 5922-32.

(50) Hurst, S. J.; Lytton-Jean, A. K. R.; Mirkin, C. A. Maximizing DNA Loading on a Range of Gold Nanoparticle Sizes. *Anal. Chem.* **2006**, *78*, 8313-8318.

(51) Zhang, H.; Wang, W.; Akinc, M.; Mallapragada, S.; Travesset, A.; Vaknin, D. Assembling and ordering polymer-grafted nanoparticles in three dimensions. *Nanoscale* **2017**, *9*, 8710-8715.

(52) Reith, D.; Müller, B.; Müller-Plathe, F.; Wiegand, S. How does the chain extension of poly (acrylic acid) scale in aqueous solution? A combined study with light scattering and computer simulation. *J. Chem. Phys.* **2002**, *116*, 9100-9106.

(53) Tolan, M. *X-Ray Scattering from Soft-Matter Thin Films: Materials Science and Basic Research*. Springer-Verlag, 1999.

(54) Als-Nielsen, J. & McMorrow, D. *Elements of Modern X-ray Physics*. John Wiley & Sons, 2011.

(55) Pershan, P. S. & Schlossman, M. L. *Liquid Surfaces and Interfaces: Synchrotron X-ray Methods*. Cambridge University Press, 2012.

(56) Vaknin, D. X-Ray Diffraction Techniques for Liquid Surfaces and Monomolecular Layers. In *Characterization of Materials*; Kaufmann, E. N., Ed.; John Wiley & Sons: New York, 2012; Vol.2, pp 1393–1423.

(57) Preston, T. C.; Nuruzzaman, M.; Jones, N. D.; Mittler, S. Role of Hydrogen Bonding in the pH-Dependent Aggregation of Colloidal Gold Particles Bearing Solution-Facing Carboxylic Acid Groups. *J. Phys. Chem. C* **2009**, *113*, 14236-14244.

(58) Si, S.; Mandal, T. K. pH-Controlled Reversible Assembly of Peptide-Functionalized Gold Nanoparticles. *Langmuir* **2007**, *23*, 190-195.

(59) Swift, T.; Swanson, L.; Geoghegan, M.; Rimmer, S. The pH-Responsive Behaviour of Poly(acrylic Acid) in aqueous solution is dependent on molar mass. *Soft Matter* **2016**, *12*, 2542-2549.

(60) Han, L.; Luo, J.; Kariuki, N. N.; Maye, M. M.; Jones, V. W.; Zhong, C. J. Novel Interparticle Spatial Properties of Hydrogen-Bonding Mediated Nanoparticle Assembly. *Chem. Mater.* **2003**, *15*, 29-37.

(61) Jones, M. R.; Macfarlane, R. J.; Prigodich, A. E.; Patel, P. C.; Mirkin, C. A. Nanoparticle Shape Anisotropy Dictates the Collective Behavior of Surface-Bound Ligands. *J. Am. Chem. Soc.* **2011**, *133*, 18865-18869.

(62) Sung, W.; Wang, W.; Lee, J.; Vaknin, D.; Kim, D. Specificity and Variation of Length Scale over which Monovalent Halide Ions Neutralize a Charged Interface. *J. Phys. Chem. C* **2015**, *119*, 7130-7137.

(63) Sabbagh, I.; Delsanti, M. Solubility of Highly Charged Anionic Polyelectrolytes in Presence of Multivalent Cations: Specific Interaction Effect. *Eur. Phys. J. E* **2000**, *1*, 75-86.

(64) Reincke, F.; Kegel, W. K.; Zhang, H.; Nolte, M.; Wang, D.; Vanmaekelbergh, D.; Mohwald, H. Understanding the self-assembly of charged nanoparticles at the water/oil interface. *Physical Chemistry Chemical Physics* **2006**, *8*, 3828-3835.

(65) Bera, M. K.; Chan, H.; Moyano, D. F.; Yu, H.; Tatur, S.; Amoanu, D.; Bu, W.; Rotello, V. M.; Meron, M.; Kral, P.; Lin, B.; Schlossman, M. L. Interfacial Localization and Voltage-Tunable Arrays of Charged Nanoparticles. *Nano Letters* **2014**, *14*, 6816-6822.

(66) Hua, X.; Bevan, M. A.; Frechette, J. Reversible Partitioning of Nanoparticles at an Oil-Water Interface. *Langmuir* **2016**, *32*, 11341-11352.

TOC Graphic

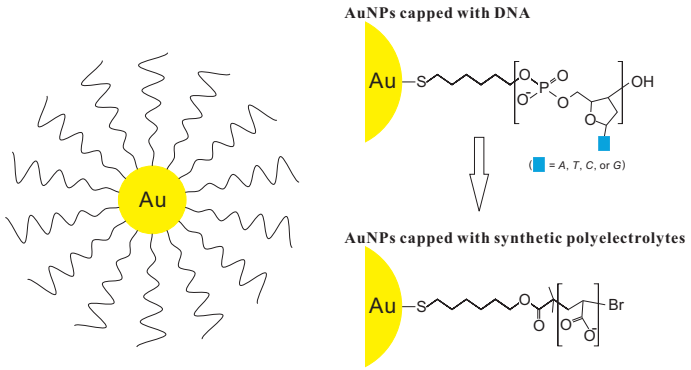
Au
AuNPs capped with DNA
Au
S
O
O
P
O
O
OH
O
(■ = A, T, C, or G)
AuNPs capped with synthetic polyelectrolytes
Au
S
O
O
O
O
Br

Supporting information

Interfacial Self-Assembly of Polyelectrolyte-Capped Gold Nanoparticles

Honghu Zhang,[†] Srikanth Nayak,[‡] Wenjie Wang,[¶] Surya Mallapragada,[‡] David Vaknin[§,*]

†*Ames Laboratory, and Department of Materials Science and Engineering, Iowa State University, Ames, Iowa 50011, United States*

†*Ames Laboratory, and Department of Chemical and Biological Engineering, Iowa State University, Ames, Iowa 50011, United States*

¶ *Division of Materials Sciences and Engineering, Ames Laboratory, USDOE, Ames, Iowa 50011, United States*

§*Ames Laboratory, and Department of Physics and Astronomy, Iowa State University, Ames, Iowa 50011, United States*

1. Synthesis and characterization of PAA

The reaction procedure for synthesis of alkylthiol-terminated PAA is shown in Fig. 2. The reaction products at different stages were characterized by ^{1}H NMR spectroscopy using a Varian VXR-300 MHz NMR spectrometer, with deuterated chloroform or water as the solvents. Molecular weight and PDI of the as-synthesized $[\mathrm{PtBA{-}R{-}S}]_2$ were estimated by gel permeation chromatography (GPC) with an RI and UV absorption detector assembly. Tetrahydrofuran was used as the solvent for all the solvents at 40 °C, at a flow rate of 1.0 mL/min. Polystyrene standards were used for obtaining the calibration curve.

Synthesis of PAA-C6

NMR results:

^{1}H NMR ($CDCl_3$) δ (ppm)

C6-Initiator: 4.2 ($-CH_2-C\mathbf{H}_2-O-CO-$), 2.6–2.7 ($-C\mathbf{H}_2-S-S-$), 1.8–2.0 ($Br-C(C\mathbf{H}_3)_2-$),

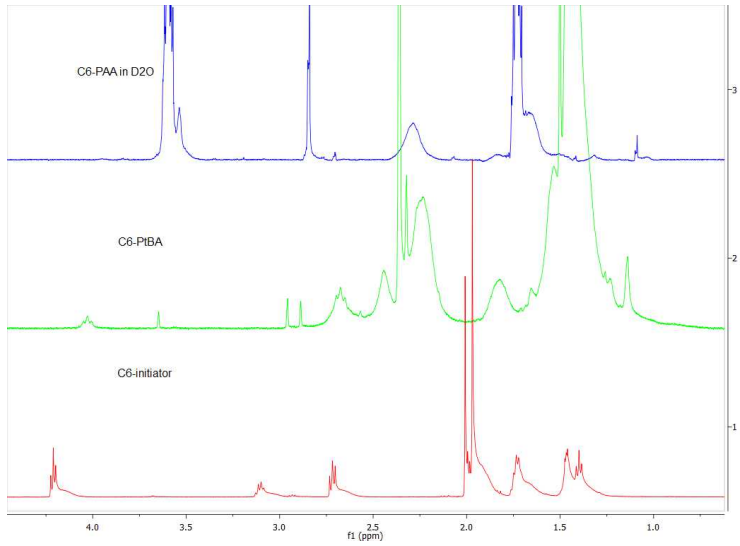

Figure S1: ^{1}H NMR spectra of the ATRP initiator ([Br$(CH_3)_2$C−COO−$(CH_2)_6$−S]$_2$), the reaction intermediate ([PtBA−C6−S]$_2$), and the product ([PAA−C6−S]$_2$) for synthesis of the PAA-C6 disulfide.

1.6–1.7 (−C**H**$_2$−CH$_2$−S−S−), 1.3–1.5 (−CH$_2$−C**H**$_2$−CH$_2$−).

C6-PtBA : 4.0 (−CH$_2$−C**H**$_2$−O−CO−), 2.6–2.7 (−C**H**$_2$−S−S−), 2.2–2.5 (−CH$_2$−C**H**(COO−tBA)−C 1.7–1.9 (−C**H**$_2$−CH(COO−tBA)−), 1.2–1.6 (Br−C(C**H**$_3$)$_2$−, −C**H**$_2$−CH$_2$−S−S−, −CH$_2$−C**H**$_2$−CH$_2$−, −CH$_2$−CH(COO−**tBA**)).

^{1}H NMR (D2O) δ (ppm)

C6-PAA : 2.7 (−C**H**$_2$−S−S−), 2.2–2.4 (−CH$_2$−C**H**(COOH)−), 1.4–1.9 (−C**H**$_2$−CH(COOH)−, −C**H**$_2$−CH$_2$−S−S−, −CH$_2$−C**H**$_2$−CH$_2$−).

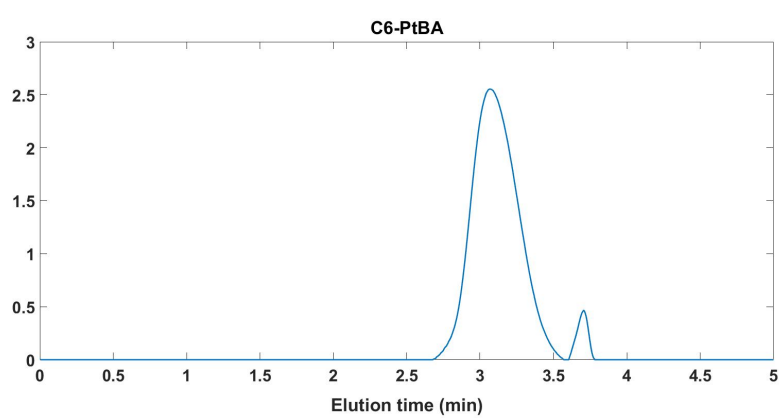

Figure S2: GPC Chromatogram of the as-synthesized [PtBA−C6−S]$_2$. It shows a M_n of ∼10,400 Da with a PDI of 1.2.

Due to the overlapping peaks of poly(acrylic acid) and the initiator, NMR is not suitable

for determining the molecular weight of the polymer. GPC results with $[PtBA{-}C6{-}S]_2$ indicate a M_n of ∼10,400 Da corresponding to ∼38 tBA units. Thus, the M_n of the as-synthesized $[PAA{-}C6{-}S]_2$ is ∼6100 Da.

Synthesis of PAA-C9

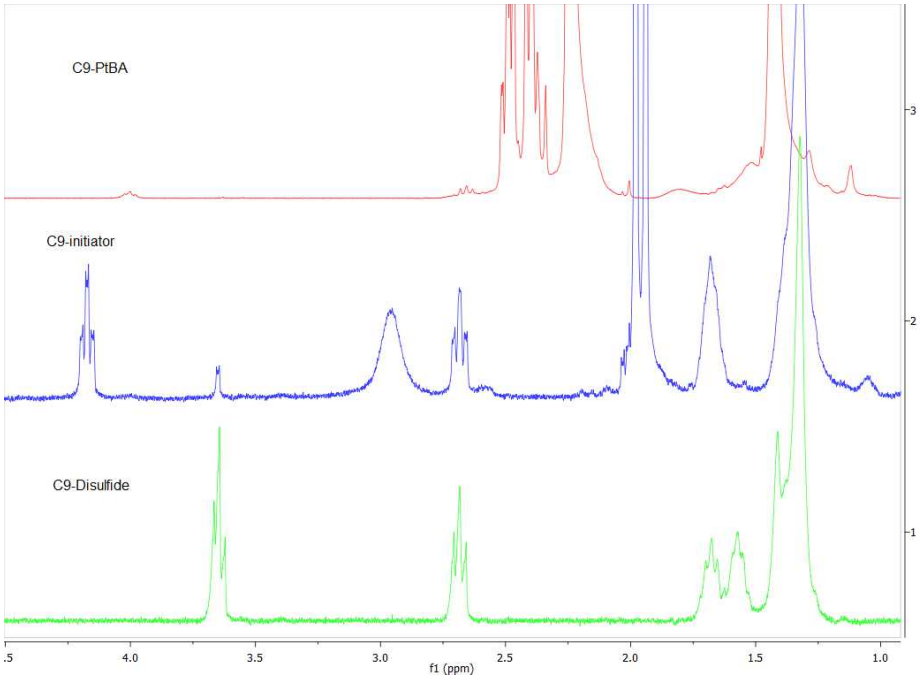

Figure S3: ^{1}H NMR spectra of the C9 disulfide ($[HO{-}(CH_2)_9{-}S]_2$), the ATRP initiator ($[Br(CH_3)_2C{-}COO{-}(CH_2)_9{-}S]_2$) and the reaction intermediate ($[PtBA{-}C_9{-}S]_2$) for synthesis of the PAA-C9 disulfide.

^{1}H NMR ($CDCl_3$) δ (ppm)

C9-disulfide: 3.6–3.7 ($HO{-}C\mathbf{H}_2{-}CH_2{-}$), 2.6–2.7 ($-C\mathbf{H}_2{-}S{-}S{-}$), 1.6–1.7 ($-C\mathbf{H}_2{-}CH_2{-}S{-}S{-}$), 1.5–1.6 ($HO{-}CH_2{-}C\mathbf{H}_2{-}CH_2{-}$), 1.3–1.5 ($-CH_2{-}C\mathbf{H}_2{-}CH_2{-}$)

C9-Initiator: 4.2 ($-CH_2{-}C\mathbf{H}_2{-}O{-}CO{-}$), 2.6–2.7 ($-C\mathbf{H}_2{-}S{-}S{-}$), 1.8–2.0 ($Br{-}C(C\mathbf{H}_3)_2{-}$), 1.6–1.7 ($-C\mathbf{H}_2{-}CH_2{-}S{-}S{-}$), 1.3–1.5 ($-CH_2{-}C\mathbf{H}_2{-}CH_2{-}$).

C9-PtBA : 4.0 ($-CH_2{-}C\mathbf{H}_2{-}O{-}CO{-}$), 2.6–2.7 ($-C\mathbf{H}_2{-}S{-}S{-}$), 2.2–2.5 ($-CH_2{-}C\mathbf{H}(COO{-}tBA){-}C$ 1.7–1.9 ($-C\mathbf{H}_2{-}CH(COO{-}tBA){-}$), 1.2–1.6 ($Br{-}C(C\mathbf{H}_3)_2{-}$, $-C\mathbf{H}_2{-}CH_2{-}S{-}S{-}$, $-CH_2{-}C\mathbf{H}_2{-}CH_2{-}$, $-CH_2{-}CH(COO{-}\mathbf{tBA})$).

The GPC result with the as-synthesized $[PtBA{-}C9{-}S]_2$ shows a M_n of ∼2,400 corresponding to ∼7 tBA units. Thus, the M_n of the $[PAA{-}C9{-}S]_2$ is ∼1630 Da.

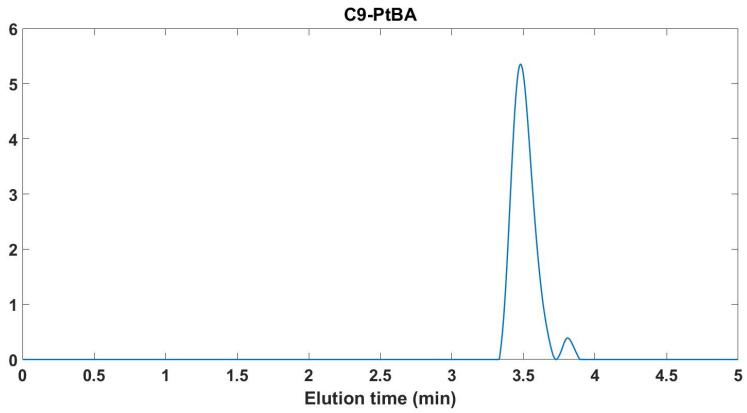

Figure S4: GPC Chromatogram of the as-synthesized $[\mathrm{PtBA-C9-S}]_2$. It shows the polymer has a M_n of ∼2400 Da with a PDI of 1.08.

2. Characterization of PAA-AuNPs in bulk

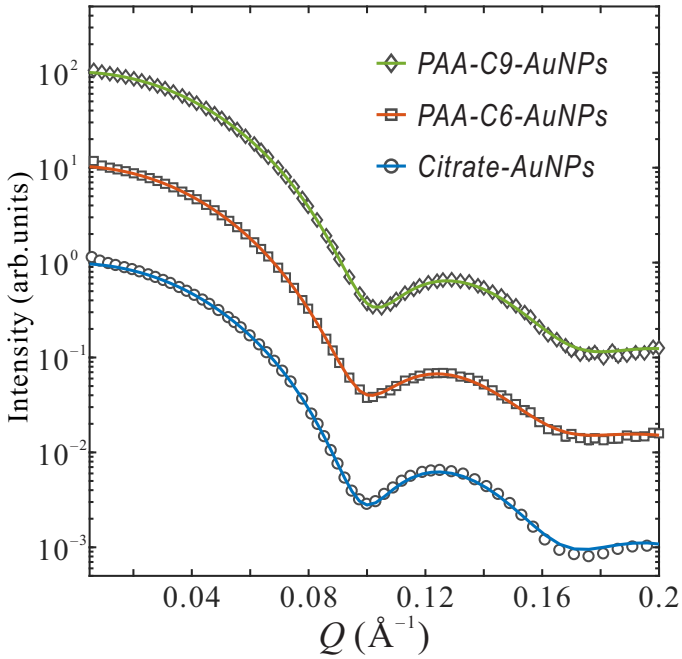

Figure S5: SAXS intensity profiles of aqueous suspension of citrate-stabilized AuNPs (circles), PAA-C6-AuNPs (squares), and PAA-C9-AuNPs (diamonds). The solid lines are best fits using a form factor of spherical particles with an assumption that the size polydispersity obeys a Gaussian distribution. The plots are vertically shifted for clarity.

The small-angle X-ray scattering is utilized to determine the size of citrate-stabilized AuNPs and PAA-capped AuNPs. The mean diameters and size distributions are determined by fitting the scattering profiles with form factors calculated using assumptions that the AuNPs are perfect hard spheres and their size distributions obey a Gaussian function. As

shown in Fig. S5, the nanoparticle size distributions estimated by the best fits are $D = 8.9 \pm 0.8$ nm (citrate-AuNPs), 8.8 ± 0.9 nm (PAA-C6-AuNPs) and 8.6 ± 0.8 nm (PAA-C9-AuNPs). These results show that the scattering is insensitive to the polyelectrolyte shell capped on AuNP cores, suggesting that the electron density of PAA shells in solution is very close to that of aqueous media surrounding them. The ED profiles extracted from XRR for the Gibbs monolayers show a stratum with a thickness of 8–10 nm, which is consistent with the core size of PAA-AuNPs. This confirms that the PAA-AuNPs self-assemble into mono-particle layers.

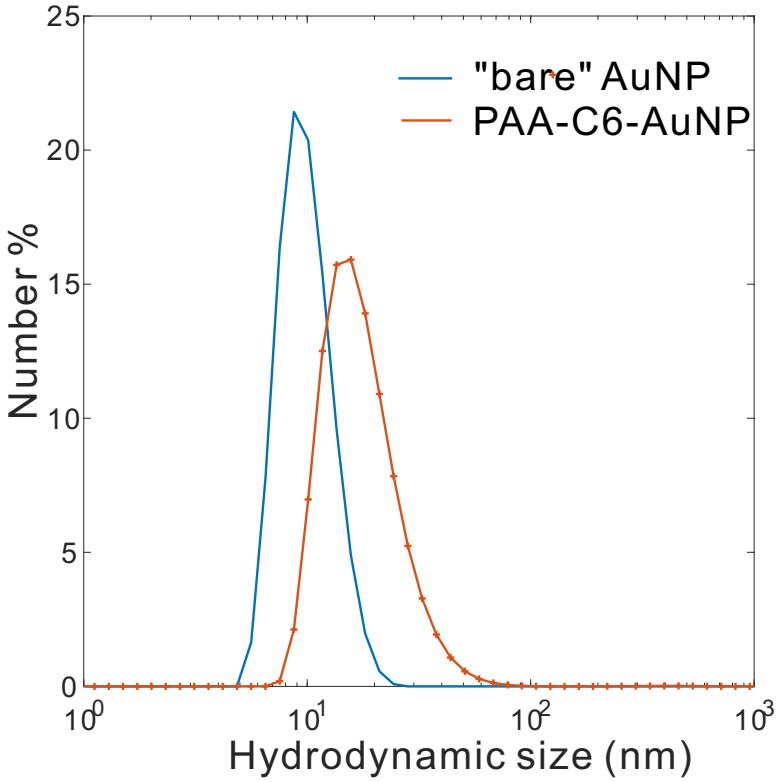

Figure S6: Dynamic light scattering (DLS) of bare AuNPs and PAA-C6-AuNPs at neutral pH showing increase in hydrodynamic diameter after capping the AuNPs.

Dynamic light scattering is used to determine the hydrodynamic size (D_h) of PAA-capped AuNPs. As shown in Fig. S6, the hydrodynamic size is dramatically increased from ∼9 nm to ∼27 nm after grafting PAA on AuNPs.

As theoretically documented in other system of polymer-grafted NPs (e.g., polyethylene glycol-capped AuNPs), the hydrodynamic size D_h of a given polymer-capped NP with a core

size of D is expressed as[46,51]

$$\left(\frac{D_h}{D}\right)^2 = 1 + 4\frac{R_{max} b \sigma^{1/2}}{D}(2w_0)^{1/4} \ , \tag{S1}$$

where b is the Kuhn length of the capped polymer, R_{max} is the contour length of PAA polymer and is given by $R_{max} = 2l_{cc}\sin(\theta/2)N_r = 0.252N_r$ nm ($l_{cc} = 1.54$ Å being the C–C bond length, $\theta = 109.5°$ being the tetrahedral C–C bond angle, N_r being the number of AA monomers in the given PAA polymer), σ is the grafting density, and w_0 is a dimensionless three body interaction, where we use the Flory result $w_0 = 1/6$, so that $(2w_0)^{1/4} = 0.76$. This model allows us to estimate the grafting density of PAA on AuNPs based on the measured hydrodynamic size.

Here, we assume that PAA is an ideal chain and obeys $R_g^2 = R_{max}b/6$, where R_g is the radius of gyration. Using the reported values of R_g, we estimate $b = 4.65$ nm (average from four PAA polymers with various lengths).[52] In this study, for PAA-C6-AuNPs, $D = 8.8$ nm (based on SAXS), $D_h = 27$ nm, and $R_{max} = 9.58$ nm for PAA-C6. Thus, the grafting density is estimated to be $\sigma = 0.30$ nm^{-2}. Correspondingly, the number of PAA chains per nanoparticle is $n = \sigma\pi D^2 = 73$ chains per particle. It is worth noting that the grafting number of thiolated ssDNA for AuNPs with the diameter of 10 nm is reported to be 40–60 chains per particle.[40,41] This result rules out the probability of agglomeration of PAA-AuNPs driven by low ligand loading on the NPs.

3. pH- and $MgCl_2$-induced interfacial assembly of PAA-AuNPs

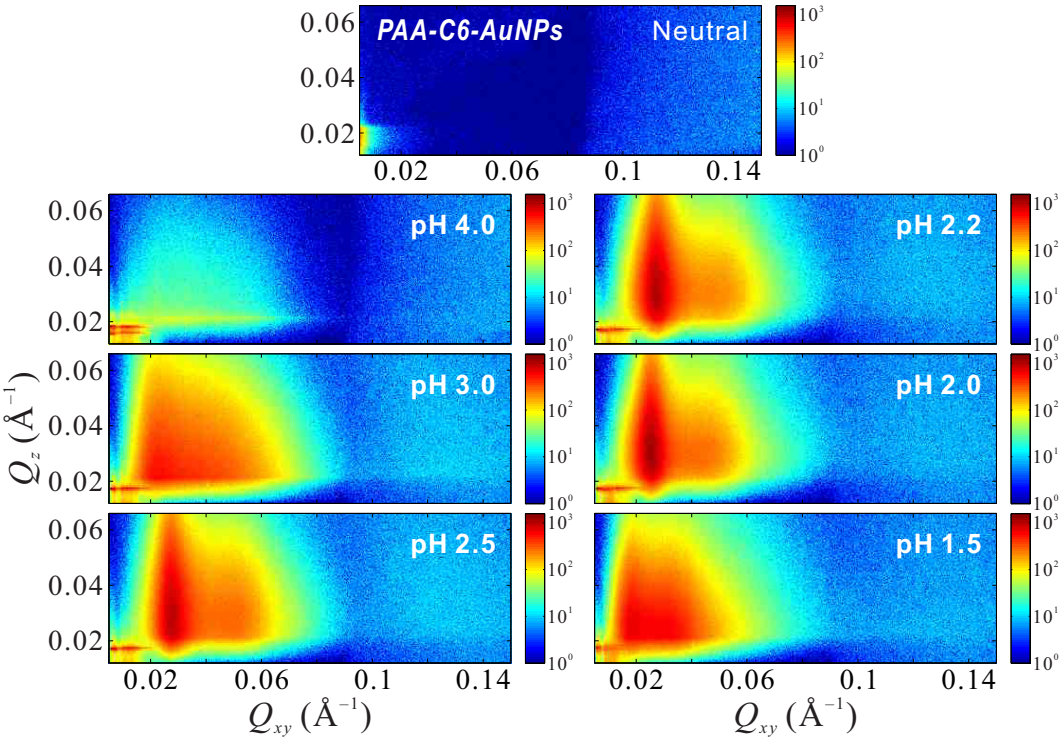

Figure S7: In-plane structural evolution of Gibbs monolayers of PAA-C6-AuNPs at the vapor–liquid interfaces at various pH levels. The GISAXS patterns are displayed as functions of Q_{xy} and Q_z on logarithmic scales under different experimental conditions as indicated.

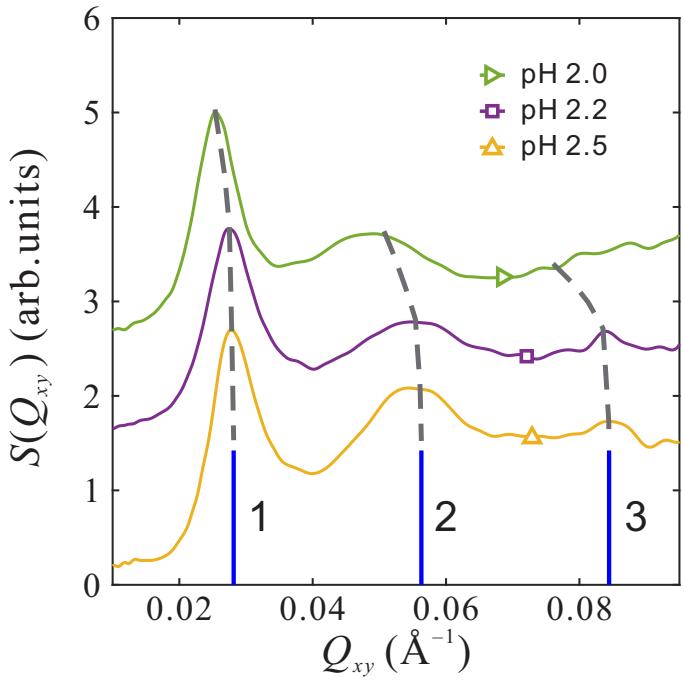

Figure S8: Structure factor $S(Q_{xy})$ extracted from the horizontal linecut profiles for the GISAXS patterns from Gibbs monolayers of PAA-C6-AuNPs at pH = 2.0–2.5. The relative peak-position-ratio with respect to the fundamental diffraction peak is close to $Q_i/Q_1 \approx 1 : 2 : 3$ (i = 1, 2, 3), indicating presence of a 1D string-like structure, i.e., a linear arrangement of surface-adsorbed nanoparticles into chains with roughly equal spacing $d_L = 2\pi/Q_1$. The linecut is along Q_{xy} direction at Q_z = 0.020 Å^{-1} integrated over Q_z range 8.5 $\times 10^{-3}$ Å^{-1} at low Q_{xy} range (0.01–0.09 Å^{-1}). The form factor profile used in the data analysis was measured from pure PAA-C6-AuNPs dispersed in aqueous bulk solution using SAXS at 12ID-B at APS. The plots are vertically shifted for clarity.

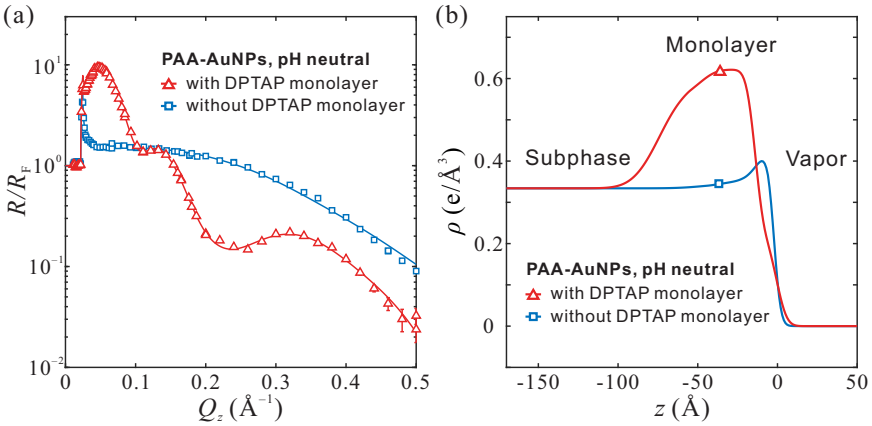

Figure S9: X-ray reflectivity of PAA-C6-AuNP suspension at neutral pH in the absence and presence of the DPTAP monolayer. (a) Normalized XRR data R/R_F for the DPTAP monolayer spread on the subphase containing PAA-C6-AuNPs and pure subphase. (b) Representative best-fit electron density profiles along surface normal direction that regenerate R/R_F (solid lines) in (a).

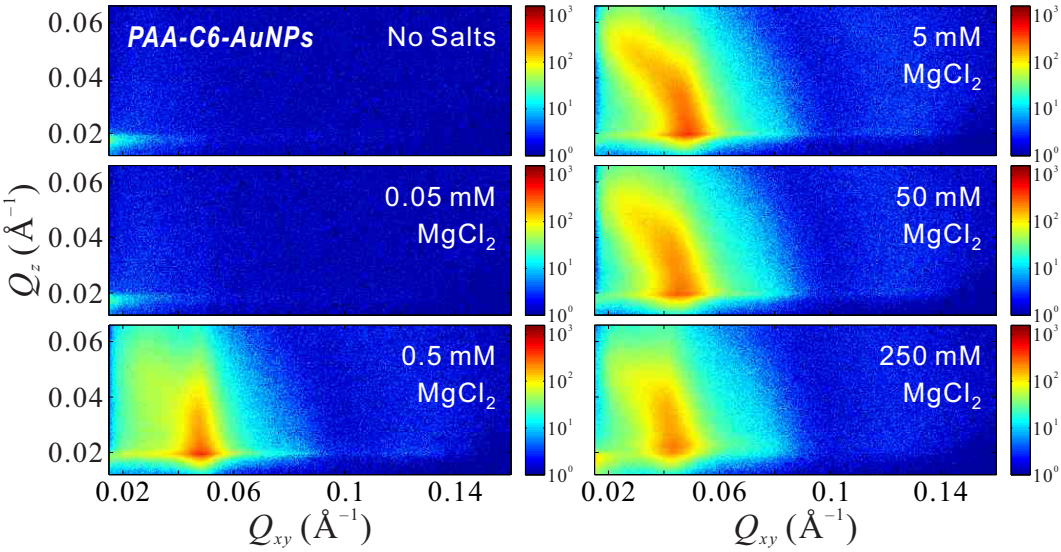

Figure S10: In-plane structural evolution of Gibbs monolayers of PAA-C6-AuNPs at the vapor–liquid interfaces in the absence and in the presence of various amounts of $MgCl_2$ (0–250 mM). The GISAXS patterns are displayed as functions of Q_{xy} and Q_z on logarithmic scales under different experimental conditions as indicated.

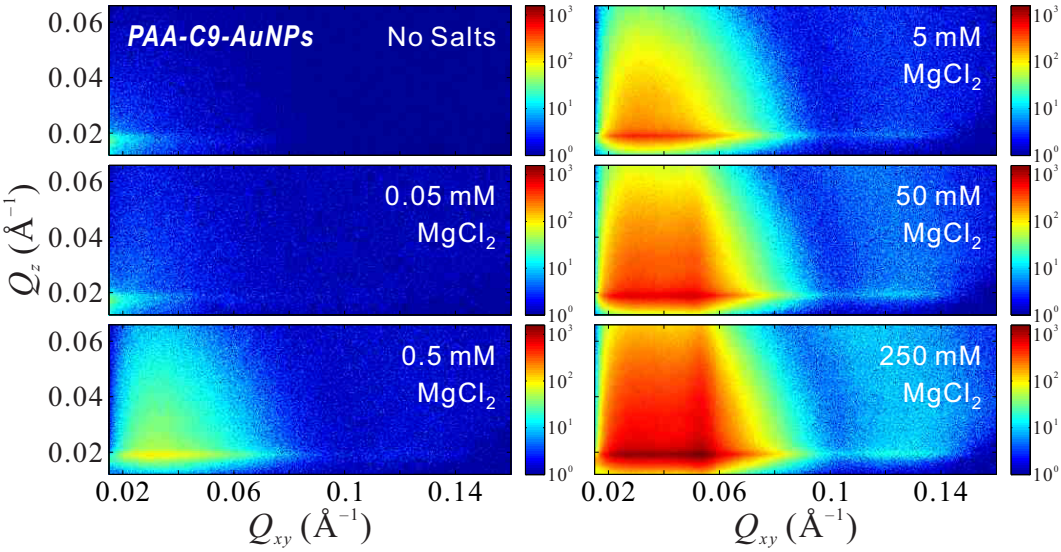

Figure S11: In-plane structural evolution of Gibbs monolayers of PAA-C9-AuNPs at the vapor–liquid interfaces in the absence and in the presence of various amounts of $MgCl_2$ (0–250 mM). The GISAXS patterns are displayed as functions of Q_{xy} and Q_z on logarithmic scales under different experimental conditions as indicated.

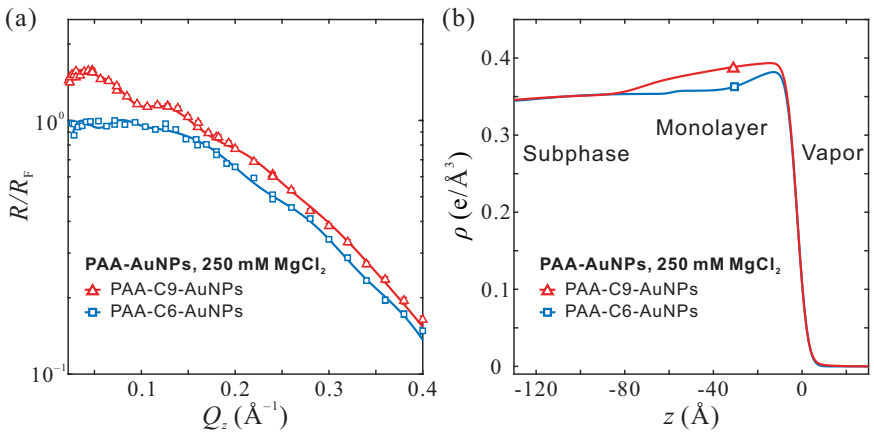

Figure S12: X-ray reflectivity of PAA-C6-AuNP and PAA-C9-AuNP suspensions in the presence of 250 mM $MgCl_2$. (a) Normalized XRR data R/R_F for the interfacial assemblies of PAA-C6-AuNPs and PAA-C9-AuNPs induced by $MgCl_2$ as indicated. (b) Representative best-fit electron density profiles along surface normal direction that regenerate R/R_F (solid lines) in (a).

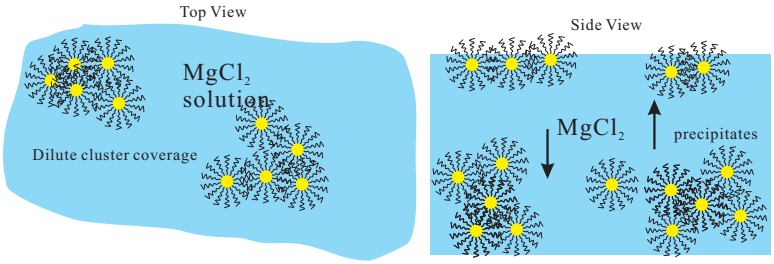

Figure S13: Illustration of the arrangement of PAA-AuNPs at the vapor/solution interface after adding $MgCl_2$ to the solution. Dilute clusters give rise to GISAXS, however the coverage is very low thus the X-ray reflectivity is dominated by the scattering from the bare solution.

4. A comment on the formation of Gibbs Monolayer

In this manuscript, we use the term Gibbs monolayer (ML) to describe a spontaneously formed monolayer from a suspension of a polyelectrolyte-capped AuNPs by manipulation of the solution (pH or salt). By contrast, a Langmuir ML is created by spreading amphiphilic and water-insoluble molecules directly at the air/water interface. The surfactant community generally deals with short chain amphiphilic molecules that if sufficiently long become insoluble and can form Langmuir monolayers. Here, we are dealing with PEs that are practically water soluble and only by virtue of changing pH or salt concentration induce hydrophobic character to the PE. The migration to the surface is a dynamic phenomena to a certain point, however our experience shows that under certain conditions we achieve equilibrium

or more correctly a steady state and saturated ML. For short surfactants, salt concentration lowers the CMC but does not significantly increase surface density to the point of crystallization. Also as short surfactants undergo formations of micelles, bi-continuous phases, lamellar structures, and even reverse micelles. Here, the situation is ill defined as we do not exactly know what happens at high concentrations of capped-AuNPs bulk (as it is impractical) and as the surface is fully covered (at high pH or salt concentrations), we observe precipitates.